Since January 2020 Elsevier has created a COVID-19 resource centre with free information in English and Mandarin on the novel coronavirus COVID-19. The COVID-19 resource centre is hosted on Elsevier Connect, the company's public news and information website.

Talanta 235 (2021) 122801

Contents lists available at ScienceDirect

Talanta

journal homepage: www.elsevier.com/locate/talanta

Fiber-optic label-free biosensor for SARS-CoV-2 spike protein detection using biofunctionalized long-period fiber grating

Seul-Lee Lee [a], Jihoon Kim [b], Sungwook Choi [a], Jinsil Han [a], Giwan Seo [c,d,**], Yong Wook Lee [a,b,*]

[a] Industry 4.0 Convergence Bionics Engineering, Pukyong National University, Busan, 48513, Republic of Korea
[b] School of Electrical Engineering, Pukyong National University, Busan, 48513, Republic of Korea
[c] Center for Convergent Research of Emerging Virus Infection, Korea Research Institute of Chemical Technology, Daejeon, 34114, Republic of Korea
[d] Research Center for Bioconvergence Analysis, Korea Basic Science Institute, Cheongju, 28119, Republic of Korea

ARTICLE INFO

Keywords:
COVID-19
SARS-CoV-2
Coronavirus
Surface functionalization
Long-period fiber grating
Phase shift

ABSTRACT

With COVID-19 widespread worldwide, people are still struggling to develop faster and more accurate diagnostic methods. Here we demonstrated the label-free detection of SARS-CoV-2 spike protein by employing a SARS-CoV-2 spike antibody-conjugated phase-shifted long-period fiber grating (PS-LPFG) inscribed with a CO_2 laser. At a specific cladding mode, the wavelength separation (λ_D) between the two split dips of a PS-LPFG varies with the external refractive index, although it is virtually insensitive to ambient temperature variations. To detect SARS-CoV-2 spike protein, SARS-CoV-2 spike antibodies were immobilized on the fiber surface of the fabricated PS-LPFG functionalized through chemical modification. When exposed to SARS-CoV-2 spike protein with different concentrations, the antibody-immobilized PS-LPFG exhibited the variation of λ_D according to the protein concentration, which was caused by bioaffinity binding-induced local changes in the refractive index at its surface. In particular, we also confirmed the potential of our sensor for clinical application by detecting SARS-CoV-2 spike protein in virus transport medium. Moreover, our sensor could distinguish SARS-CoV-2 spike protein from those of MERS-CoV and offer efficient properties such as reusability and storage stability. Hence, we have successfully fabricated a promising optical transducer for the detection of SARS-CoV-2 spike protein, which can be unperturbed by external temperature disturbances.

1. Introduction

The recent outbreak of novel coronavirus disease 2019 (COVID-19), caused by severe acute respiratory syndrome coronavirus 2 (SARS-CoV-2), has globally threatened human health. What was worse, it is rapidly spreading across the globe from Asia to other continents because of its rapid human-to-human transmission [1]. As of March 04, 2021, more than 114,428,211 cases of COVID-19 have been confirmed around the world, resulting in 2,543,755 deaths [2]. Since no specific drugs for COVID-19 are yet available, early diagnosis is still critical for controlling the outbreak. Thus, highly sensitive diagnostic methods capable of rapid and direct detection of SARS-CoV-2 are required to obtain worthy information that can be provided to medical teams in the treatment of COVID-19. There are ongoing efforts to develop diagnostic platforms integrated with current biosensing protocols for rapid and selective detection of the virus. As one of the promising alternatives to conventional diagnostic methods, biosensor technology has been developed and reported for the determination of SARS-CoV-2 by employing various kinds of detection platforms. For example, reverse transcription-polymerase chain reaction (RT-PCR) is a predominant diagnostic method for COVID-19 but too time-consuming to be used for on-site detection [3]. Besides, assays based on reverse transcription loop-mediated isothermal amplification (RT-LAMP) were reported for rapid detection of RNA samples extracted from SARS-CoV-2 in about 30 min [4]. More recently, a dual-functional plasmonic biosensor was reported to detect SARS-CoV-2 with a low limit of detection (LOD) of 0.22 pM and distinguish genes of SARS-CoV from ones of SARS-CoV-2 [5]. These methods are highly accurate and sensitive diagnostic technologies to detect SARS-CoV-2 but depend on the DNA detection-based method with disadvantages of the complex extraction and denaturation of viral RNA or DNA [6]. By incorporating a detection method based on antigen-antibody reaction, a graphene-based field-effect transistor

* Corresponding author. School of Electrical Engineering, Pukyong National University, Busan, 48513, South Korea.
** Corresponding author. Research Center for Bioconvergence Analysis, Korea Basic Science Institute, Cheongju, 28119, South Korea.
E-mail addresses: danielseo7@gmail.com (G. Seo), yongwook@pknu.ac.kr (Y.W. Lee).

https://doi.org/10.1016/j.talanta.2021.122801
Received 4 March 2021; Received in revised form 17 June 2021; Accepted 11 August 2021
Available online 13 August 2021

sensor was implemented to detect SARS-CoV-2 and its spike proteins with specific spike antibodies in clinical samples and discriminate SARS-CoV-2 spike protein from those of MERS-CoV [7].

In terms of optical approaches, much interest has been paid to a long-period fiber grating (LPFG), which is embodied by a periodic modulation of the refractive index of the fiber core with a period of hundreds of micrometers, as a promising platform for biosensing applications due to its superiority over other technology platforms in that it can offer some advantages such as small size, light weight, polarization independence, real-time and remote sensing capabilities, ease of fabrication, immunity to electromagnetic interference, and intrinsic sensitivity to surrounding medium refractive index (SMRI) changes [8–11]. In particular, an LPFG couples light from the fundamental guided mode to forward propagating cladding modes resulting in a transmission spectrum containing a series of attenuation bands centered at discrete resonance wavelengths where the phase-matching condition (PMC) is satisfied [12]. In general, since the PMC of an LPFG is affected by the difference between core and cladding effective refractive indices, which is strongly dependent on the SMRI, the resonance wavelength of the LPFG varies with changes in the SMRI along the fiber [13]. Considering the effect of the SMRI variation on the resonance wavelength of the LPFG, a shift in the resonance wavelength can be exploited as a biosensing indicator to detect SMRI changes induced by a biological reaction occurring on the fiber surface. Demodulation of wavelength-encoded signals is more reliable than an intensity-based interrogation system that suffers from unexpected power fluctuations caused by external perturbations [8]. To achieve high selectivity to the target analyte, the LPFG surface can be functionalized through the deposition of a selective biolayer, which can be significantly enhanced with the help of additional surface modification processes that make biological recognition elements be covalently bonded onto the surface. The biofunctionalized LPFG offers the feasibility of an LPFG-based biosensor that can detect a minute amount of analytes with a high sensitivity to the SMRI variation induced by biological activity. In brief, the interaction between the biological recognition element and the analyte on the surface of the biofunctionalized LPFG can be detected directly through observation of its resonance wavelength shift, and such a detection approach, referred to as a label-free detection, can provide the possibility of the real-time measurement associated with biological activities without suffering from the inconvenience of laborious labeling processes. To date, numerous LPFG-based biosensors have already been proposed to prove that an LPFG is a useful apparatus for the label-free detection of various types of bioanalytes. For example, a graphene oxide (GO)-coated dual-peak LPFG was presented for the detection of anti-IgG with an LOD of 7 ng/mL by analyzing quantitative variations of the wavelength separation between the dual peaks, which occur by SMRI changes induced by bioaffinity binding between the immobilized IgG and the target anti-IgG at the GO-coated interface [14]. For the specific detection of glucose, a glucose oxidase (GOD)-immobilized LPFG was implemented and showed the linear correlation between the wavelength shift of its transmission spectrum and the glucose concentration in the range of 0.1–3 mg/mL [15]. By harnessing the specific binding between bacteria and bacteriophage, *Escherichia coli* of 10^3 CFU/mL was detectable with a bacteriophage-immobilized LPFG [16], and T7 bacteriophage detection using an LPFG-based immunosensor was also achieved with an LOD of 5×10^3 PFU/mL [17]. Previous works show that LPFG-based optical biosensors can detect various types of biological targets in a label-free manner through appropriate surface biofunctionalization. However, despite the urgent need for the rapid and sensitive immunological diagnosis of COVID-19, any study on LPFG-based biosensors for the detection of SARS-CoV-2 spike protein has not been reported yet.

Here we demonstrate label-free detection of SARS-CoV-2 spike protein by employing a SARS-CoV-2 spike antibody (SSA)-conjugated phase-shifted LPFG (PS-LPFG) inscribed by CO_2 laser pulses as a biosensor head. The SSA-immobilized PS-LPFG serves as a label-free optical transducer to directly detect SARS-CoV-2 spike protein whose binding with the SSAs induces local changes in the refractive index of the bio-interaction layer. For the fabrication of a PS-LPFG, a π phase shift was introduced in the middle of an LPFG with periodical index modulation along the core of single-mode fiber (SMF). This π phase shift can convert destructive interference into constructive interference at the PMC, resulting in a splitting of a wavelength-dependent loss dip at the resonance wavelength. For two split dips with a specific cladding mode, their wavelength separation (λ_D) varies with the SMRI, although it remains virtually constant for ambient temperature variations owing to the grating formation based on CO_2 laser irradiation [18–20]. To achieve high selectivity to SARS-CoV-2 spike protein in the sensor head, the surface of the fabricated PS-LPFG was functionalized with the immobilization of antibodies against SARS-CoV-2 spike protein on its unjacketed fiber surface, and its antibody binding capability could be enhanced through premodification of the fiber surface with (3-Aminopropyl) triethoxysilane (APTES) and glutaraldehyde (GA), an efficient interface coupling agent used as a probe linker. When the PS-LPFG conjugated with SSAs was exposed to SARS-CoV-2 spike protein, it could be observed that λ_D varied with increasing antigen concentration owing to bioaffinity binding-induced changes in the refractive index at its surface. Hence, the SSA-conjugated PS-LPFG can act as a temperature-insensitive optical transducer for the detection of SARS-CoV-2 spike protein through quantitative analysis of λ_D as a function of the binding event between antigen and antibody at the fiber surface. In particular, we confirmed the potential of our sensor for clinical application by detecting SARS-CoV-2 spike protein in the virus transport medium used to collect and transport clinical virus specimens. Moreover, our sensor could distinguish SARS-CoV-2 spike protein from those of MERS-CoV and also provide the reusability and storage stability of the sensor head. Furthermore, the use of a CO_2 laser for the grating writing can considerably reduce the fabrication cost of PS-LPFGs compared with UV grating inscription, which enables the potential supply of cost-effective sensor heads. This study is the demonstration of an optical transducer based on the integration of SSAs with a PS-LPFG, enabling the sensitive and selective detection of SARS-CoV-2 spike protein in a clinical virus transport medium as well as a standard buffer while minimizing the effect of environmental temperature perturbations.

2. Materials and methods

2.1. Reagents

Hydrogen peroxide (H_2O_2), sulfuric acid (H_2SO_4), and ethanol (C_2H_5OH), used in the treatment of the PS-LPFG surface, were purchased from SAMCHUN chemicals (Seoul, Korea). In addition, (3-Aminopropyl) triethoxysilane (APTES), glutaraldehyde (GA, aqueous solution), phosphate buffered saline (1 × PBS, pH 7.4), and deionized (DI) water were purchased from Sigma-Aldrich (St. Louis, MO, USA). For transport medium, FA transport medium (FTM) was purchased from FA Inc. (Seoul, Korea). SSA (40150-R007, Sino Biological, Beijing, China) was employed to detect SARS-CoV-2 spike protein (40591-V08H, Sino Biological, Beijing, China) and MERS-CoV spike antigen protein (MERSS126-R-10, Alpha Diagnostic Intl., TX, USA). NH_2-functionalized gold nanoparticles (AuNPs) (765317, Sigma-Aldrich, St. Louis, MO, USA) were used to confirm the efficiency of the surface modification of the PS-LPFG. All chemical and biochemical reagents were of analytical grade and used as received with no further purification.

2.2. Transmission characteristics of PS-LPFG

A PS-LPFG is composed of two identical sections of an LPFG with a grating length and grating period of L and Λ, respectively, between which an unperturbed region of a fiber of L_{PS} in length is inserted. The intensity transmittance of the PS-LPFG can be derived based on the coupled-mode theory with the help of the fundamental matrix method [12]. When the beam propagates through the PS-LPFG whose length is

$2L + L_{PS}$, the intensity transmittance I of the PS-LPFG can be depicted by

$$I = I_{co} + I_{cl,m} - 2\sqrt{I_{co}I_{cl,m}}\cos\left\{2\tan^{-1}\left[\frac{\delta}{\sqrt{\delta^2+\kappa^2}}\tan\left(\sqrt{\delta^2+\kappa^2}\cdot L\right)\right] + (\beta_{co}-\beta_{cl,m})L_{PS}\right\}, \quad (1)$$

where I_{co} and $I_{cl,m}$ are the normalized intensities of the core and the mth cladding modes, respectively, and δ is the phase mismatch given by $\delta = (\beta_{co} - \beta_{cl,m} - 2\pi/\Lambda)/2$. β_{co} (= $2\pi n_{co}/\lambda$) and $\beta_{cl,m}$ (= $2\pi n_{cl,m}/\lambda$) are the propagation constants of the core and the mth cladding modes, respectively. n_{co} and $n_{cl,m}$ are the refractive indices of the core and the mth cladding modes, respectively, and λ is the free-space wavelength. κ is the coupling coefficient given by $\omega\varepsilon_0 n_{co}\Delta n\gamma/2$, where ω, ε_0, Δn, and γ are the optical angular frequency, the dielectric constant of vacuum, the average refractive index modulation in the core, and the overlap integral of two modes (i.e., the transverse fields of the core and the mth cladding modes) over the cross-section, respectively. If L_{PS} becomes $(1 + 1/2)\Lambda$, or a 1.5-fold the grating period, $(\beta_{co} - \beta_{cl,m})L_{PS} = 2\pi(n_{co}/\lambda - n_{cl,m}/\lambda)$ $(3\Lambda/2)$ approaches 3π near the resonance wavelength $\lambda_{res} = (n_{co} - n_{cl,m})\Lambda$ where the PMC (i.e., $\delta = 0$) is satisfied, and then the intensity transmittance I near the resonance wavelength λ_{res} is reduced to

$$I = I_{co} + I_{cl,m} + 2\sqrt{I_{co}I_{cl,m}}\cos\left\{2\tan^{-1}\left[\frac{\delta}{\sqrt{\delta^2+\kappa^2}}\tan\left(\sqrt{\delta^2+\kappa^2}\cdot L\right)\right]\right\}, \quad (2)$$

which indicates that the transmission spectrum of the π-PS-LPFG has two attenuation bands symmetrically split about the resonance wavelength λ_{res}.

2.3. CO_2-laser-based grating fabrication and spectral characteristic of fabricated PS-LPFG

Fig. 1(a) shows a schematic diagram of the experimental setup to inscribe a PS-LPFG on SMF (Corning SMF-28) using a 10.6 μm CO_2 laser (Synrad FSVI30SAC) with the line-by-line technique. For the grating fabrication, an unjacketed SMF segment was mounted on a motorized linear stage, and we fixed one end of the SMF segment on the linear stage and suspended a weight of 18 g from its other end to apply slight longitudinal tension to the fiber and ensure exact grating periods. The output beam of the CO_2 laser was focused by an $f-\theta$ lens contained in a 2D optical scanner (MINISCAN), and the focused laser beam irradiating one side of the unjacketed SMF was precisely steered with the help of the optical scanner to achieve a desired index modulation profile of a PS-LPFG. The CO_2-laser-based grating inscription setup implemented for the fabrication of PS-LPFGs can be seen in Supplementary Fig. S1. During the inscription of PS-LPFGs, the focused laser beam with a spot size of ~68 μm was scanned along the fiber with an average optical power of ~2.78 W, a scanning speed of 50 mm/s, and 10 scanning cycles. During one laser scanning cycle, the laser beam was scanned onto the fiber in both directions perpendicular to the longitudinal direction of the fiber (i.e., from top to bottom and then from bottom to top without lateral movements) to make each index-modulated layer. The grating pitch of the fabricated PS-LPFG was 588 μm, and the number of its laser-engraved points was 24 with two engraved points having a 1.5-fold grating pitch (= 1.5 × 588 μm) in the middle of the grating, ending up with a grating length of ~13.82 mm. In-situ monitoring of the transmission spectrum of the fabricated PS-LPFG was done with a broadband light source (BLS, Fiberlabs FL7701) and an optical spectrum analyzer (OSA, Yokogawa AQ6370C), which were connected to either end of the fabricated grating.

Fig. 1(b) shows a side-view microscopic image of the central section of the fabricated PS-LPFG, and one laser-engraved point in the grating can be clearly seen in the inset. It can be confirmed from the figure that two engraved points with a 1.5-fold grating pitch are well-structured along the periodically formed grating. Fig. 1(c) shows the transmission spectrum of the fabricated PS-LPFG, measured at room temperature without any applied external perturbations. As seen in the figure, the fabricated grating has two split attenuation bands at two different dip wavelengths, where shorter and longer wavelengths are denoted by λ_1 (= ~1492.09 nm) and λ_2 (= ~1569.17 nm), respectively. The inter-dip wavelength separation between both dips, referred to hereafter as λ_D (= $\lambda_2 - \lambda_1$), is exploited as a sensor indicator to quantify

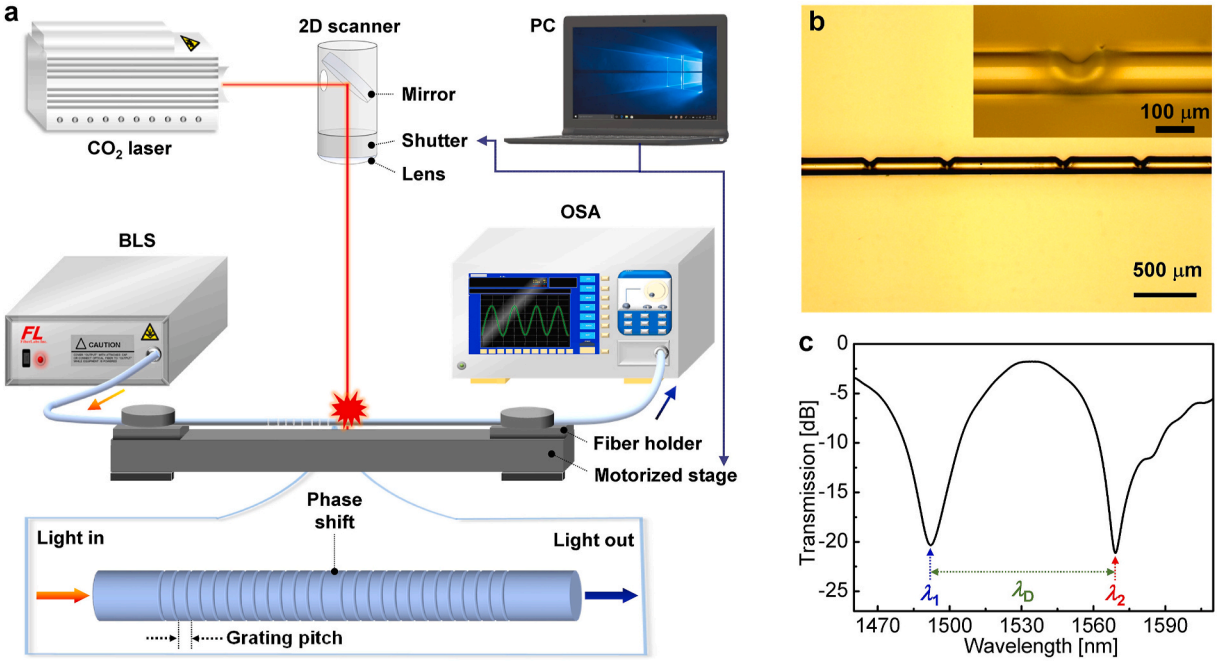

Fig. 1. Fabrication and spectral characteristic of PS-LPFG. (a) Schematic illustration of fabrication setup of PS-LPFG inscribed by CO_2 laser. (b) A side-view microscope image of fabricated PS-LPFG. The inset of (b) shows one laser-engraved point in the fabricated PS-LPFG. The scale bars in (b) and its inset indicate 500 and 100 μm, respectively. (c) Transmission spectrum of fabricated PS-LPFG, measured at room temperature without any applied external perturbations. Two attenuation dips at λ_1 and λ_2, split by a phase shift of π, are separated by $\lambda_D = \lambda_2 - \lambda_1$ in wavelength.

SMRI changes on the surface of the PS-LPFG where biological reactions primarily take place. The band rejection ratios of the two attenuation dips were measured to be ~18.6 dB at λ_1 and ~19.3 dB at λ_2, and the insertion loss of the PS-LPFG was measured to be ~1.7 dB. The two attenuation dips are associated with the same cladding mode (LP_{05}). For this cladding mode, an SMRI variation makes λ_1 and λ_2 change in opposite directions ending up with a change in λ_D, although an ambient temperature variation induces an equal displacement in λ_1 and λ_2 with λ_D remained unchanged. By harnessing these SMRI and temperature responses of the sensor indicator (λ_D), which are distinctly different, therefore, the temperature-insensitive detection of SMRI changes can be accomplished using the fabricated PS-LPFG. In particular, the use of λ_D as the sensor indicator offers a higher sensitivity to the proposed sensor because the SMRI-induced displacement of λ_D becomes larger than those of individual dip wavelengths (λ_1 or λ_2) owing to the SMRI-induced dip movement in opposite directions.

2.4. Immobilization of SSA on PS-LPFG surface

Fig. 2(a) illustrates the immobilization steps of SSA through the surface functionalization of the fabricated PS-LPFG. The entire procedure was carried out at room temperature according to the following steps. First of all, the fabricated PS-LPFG was cleaned with freshly prepared piranha solution, which is a mixture of concentrated H_2SO_4 with H_2O_2 in a ratio of 3:1 (v/v or by volume), at room temperature for 30 min to remove organic contaminants. After the cleaning process, the PS-LPFG was thoroughly rinsed three times with copious amounts of DI water. To create functional amine groups (-NH_2) on the surface of the PS-LPFG, APTES was employed as a soluble silane coupling reagent, and the hydroxylated surface of the PS-LPFG was dipped in a freshly prepared 5 % (v/v) APTES solution (dissolved in ethanol) for 2 h at room temperature. Then, the PS-LPFG was rinsed successively with ethanol and DI water several times to completely remove any residues of compounds, followed by thermal annealing for 1 h at 120 °C. After the formation of the amine-functionalized surface, the PS-LPFG was subsequently treated with 2 % (v/v) GA solution for 3 h at room temperature to activate glutaraldehyde cross-linking. The aldehyde groups (-CHO) of GA, formed through this GA treatment, can be bound with the -NH_2 groups of SSA. Finally, the functionalized PS-LPFG, ready for amine cross-linking, was exposed to 100 μg/mL SSA for 3 h at room temperature.

2.5. Surface characterization of functionalized PS-LPFG

To confirm the efficiency of the surface functionalization for SSA conjugation, NH_2-functionalized AuNPs were applied to the PS-LPFG functionalized with APTES and subsequently activated with GA. To investigate the surface coverage of the PS-LPFG anchored with AuNPs, scanning electron microscopy (SEM, Tescan Mira 3, Seoul, Korea) was utilized. To provide a visual comparison, a surface SEM image of a bare PS-LPFG (without functionalization) was also scrutinized as a control examination, which showed a smooth surface of the bare fiber as seen in Fig. 2(b). Fig. 2(c) displays an SEM image acquired after the deposition of the NH_2-functionalized AuNPs on the treated PS-LPFG via APTES and

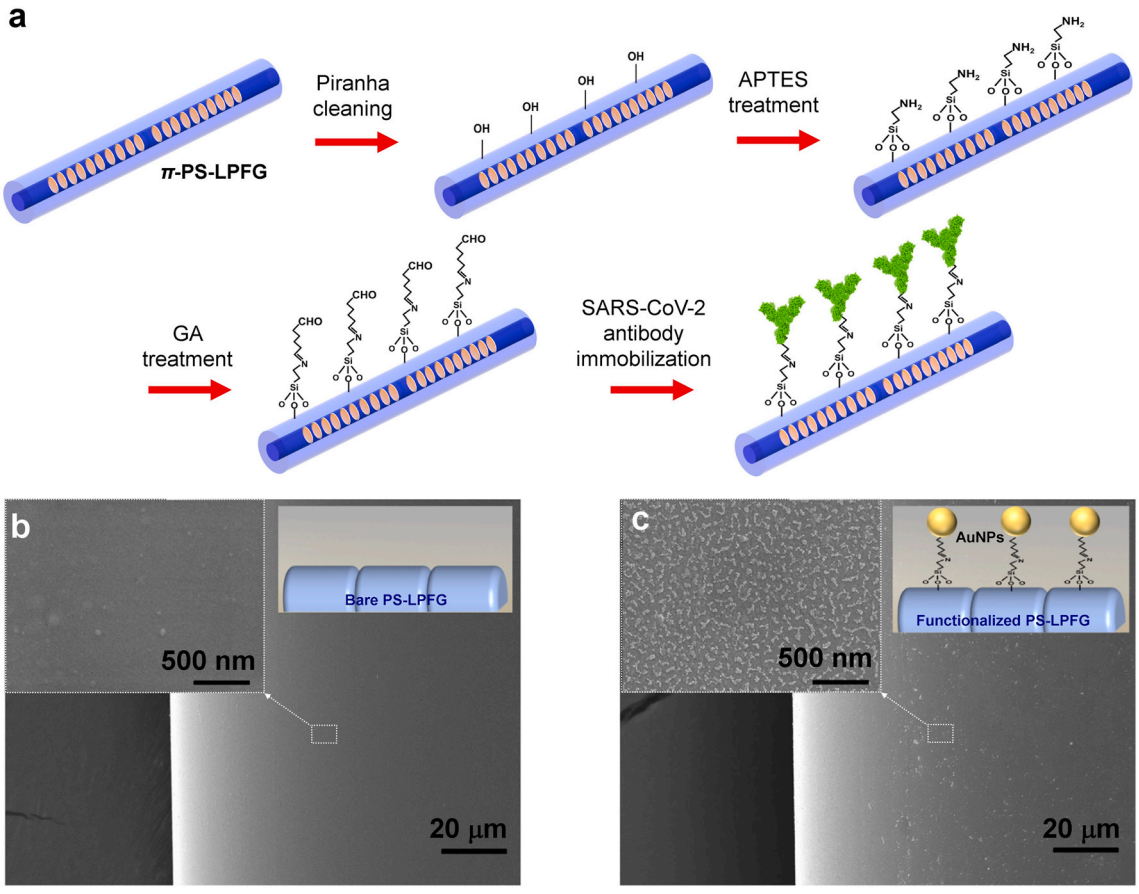

Fig. 2. SSA conjugation of fabricated PS-LPFG. (a) Schematic diagram of SSA immobilization steps through surface functionalization of fabricated PS-LPFG: Piranha cleaning, APTES treatment, GA activation, and SSA immobilization (in sequence). SEM images of (b) bare and (c) treated PS-LPFGs, acquired after deposition of NH_2-functionalized AuNPs. The insets of (b) and (c) represent the magnified images of white dotted boxes in (b) and (c), respectively, which clearly show that the AuNPs are well anchored on the surface of the functionalized PS-LPFG. The scale bars in (b) and its inset indicate 20 μm and 500 nm, respectively, and the same holds true for (c) and its inset.

GA. The insets of Fig. 2(b) and (c) represent the magnified images of white dotted boxes in Fig. 2(b) and (c), respectively, which clearly show that the AuNPs are well anchored and regularly distributed on the surface of the functionalized PS-LPFG. The different surface morphology between the SEM images in Fig. 2(b) and (c) revealed that the AuNPs were successfully bound to the treated PS-LPFG. This verifies that the surface of the PS-LPFG is effectively modified through APTES and GA treatment to conjugate SSAs on the unjacketed fiber surface. All the presented surface images were obtained by SEM operated at 10 kV.

2.6. Measurement setup for SARS-CoV-2 spike protein detection with SSA-immobilized PS-LPFG

Fig. 3 shows a schematic diagram of the experimental setup used to measure the presence of SARS-CoV-2 spike protein in buffer solutions (PBS) with the SSA-immobilized PS-LPFG. The experimental setup consists of the BLS, the OSA, and the sensor head (i.e., the SSA-immobilized PS-LPFG). To begin with, the sensor head was placed straight in the sample container with both ends fixed to minimize the bend-induced effect. In the experiment for detection of SARS-CoV-2 spike protein, the sample container containing the SSA-immobilized PS-LPFG (i.e., the sensor head) was initially filled with the PBS solution, and then a solution of SARS-CoV-2 spike protein was sequentially injected into the sample container, starting from the lowest antigen concentration (1 pg/mL) in an accumulative manner. Every time the antigen solution was dropped on the sensor head, the spectral variations of the dual dips in the transmission spectrum of the grating, induced by the interaction between antibody immobilized on the PS-LPFG and corresponding antigen, were monitored by the OSA with a resolution bandwidth of 0.02 nm and 8001 sample points. The λ_D variation in the transmission spectrum was investigated for various concentrations of SARS-CoV-2 spike protein ranging from 1 pg/mL to 100 μg/mL (i.e., 10^8 pg/mL). All measurement procedures were conducted 20 min after the sample injection at room temperature. During the measurement, the sensor head was always immersed in solution without rinsing while the antigen concentration was increased, and the injection volume of the antigen solution was very small compared with the volume of the PBS solution. So, it was confirmed that microbubbles were barely created only with the slow injection of the antigen solution. Moreover, a vacuum pump can be employed to remove microbubbles that may exist on the surface of the sensor head, but in this study these microbubbles were detached from the surface of the sensor head by simply applying light impact to the sample container using a rubber stick.

3. Experimental results and discussion

3.1. Detection of SARS-CoV-2 spike protein in standard buffer

For the performance evaluation of the fabricated sensor, we investigated its response to antigen protein. Fig. 4(a) shows superposed transmission spectra measured for various concentrations of SARS-CoV-2 spike protein. Magnified plots of Fig. 4(a) near the two attenuation minima with dip wavelengths of λ_1 and λ_2 are given in Fig. 4(b) and (c), respectively. As the concentration of antigen protein increases from 1 pg/mL to 100 μg/mL, the attenuation dips at λ_1 and λ_2 move towards shorter and longer wavelength regions, as seen in Fig. 4(b) and (c), respectively, leading to a change in λ_D of ~1.39 nm. As a function to measure changes in the SMRI, induced by antigen-antibody interactions occurring at the surface of the SSA-conjugated PS-LPFG, this λ_D variation can be understood by considering a change in the phase shift $\Delta\varphi$ given by $(\beta_{co} - \beta_{cl,m})L_{PS} = 2\pi(n_{co}/\lambda - n_{cl,m}/\lambda)$ $(3\Lambda/2)$. Based on the optical waveguide theory for a cylindrical waveguide, in a specific range of the refractive index, an increase in the SMRI can decrease the effective refractive index $n_{cl,m}$ of the mth cladding mode, and the same is true for the LP_{05} cladding mode specific to the fabricated PS-LPFG. This SMRI-induced decrease of $n_{cl,m}$ leads to the increase of $\Delta\varphi$, ending up with the increase of λ_D [21]. In brief, a bioaffinity binding-induced increase in the SMRI is presumed to be responsible for an increase in λ_D. In light of this, the wavelength variation of λ_D, measured in the SSA-immobilized PS-LPFG, can serve as a direct indicator of SARS-CoV-2 spike protein concentration.

To further explore the normalized sensitivity of the SSA-conjugated PS-LPFG to the SARS-CoV-2 spike protein concentration (ranging from 1 to 10^8 pg/mL), its spectral response was quantified using detuning parameters $\Delta\lambda_{1,det}$, $\Delta\lambda_{2,det}$, and $\Delta\lambda_{D,det}$ defined as $100 \times (\Delta\lambda_1/\lambda_{1,0})$, $100 \times (\Delta\lambda_2/\lambda_{2,0})$, and $100 \times (\Delta\lambda_D/\lambda_{D,0})$, respectively. $\lambda_{1,0}$, $\lambda_{2,0}$, and $\lambda_{D,0}$ are λ_1, λ_2, and λ_D of the unperturbed sensor head, and $\Delta\lambda_1$, $\Delta\lambda_2$, and $\Delta\lambda_D$ are the wavelength deviations from $\lambda_{1,0}$, $\lambda_{2,0}$, and $\lambda_{D,0}$, occurred in the perturbed sensor head, respectively. Fig. 4(d) shows the variations of the detuning parameters $\Delta\lambda_{1,det}$ and $\Delta\lambda_{2,det}$ according to the antigen protein concentration, displayed as red circles and blue squares, respectively. Likewise, the variation of $\Delta\lambda_{D,det}$ with respect to the antigen protein concentration can be found in Fig. 4(e). All data points shown in Fig. 4 (d) and (e), related with the SSA-conjugated PS-LPFG, were nonlinearly fitted based on the Hill adsorption model with a correlation coefficient (R^2) of ~0.99021. The resulting fitted curves were displayed as solid lines in the figures. Although the treated PS-LPFG shows the concentration-dependent response with relatively intrusive errors, the measured response manifests its detection capability of SARS-CoV-2 spike protein. Unlike the treated PS-LPFG, however, the detuning

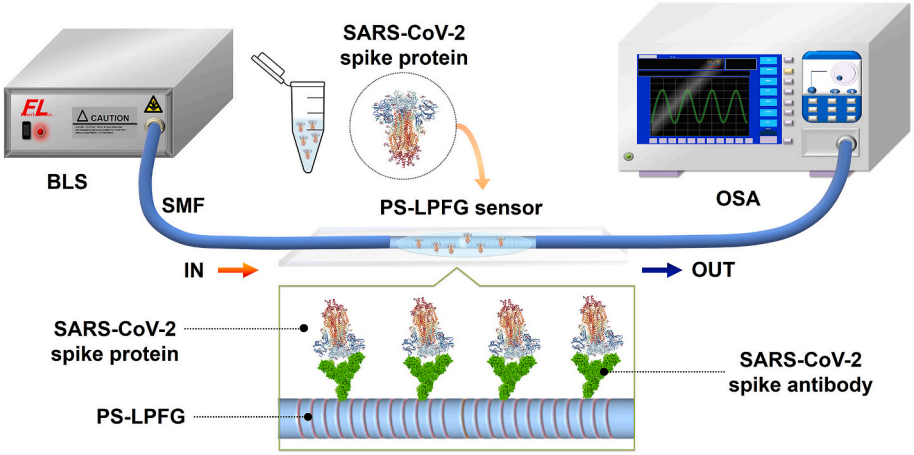

Fig. 3. Schematic diagram of experimental setup for detection of SARS-CoV-2 spike protein.

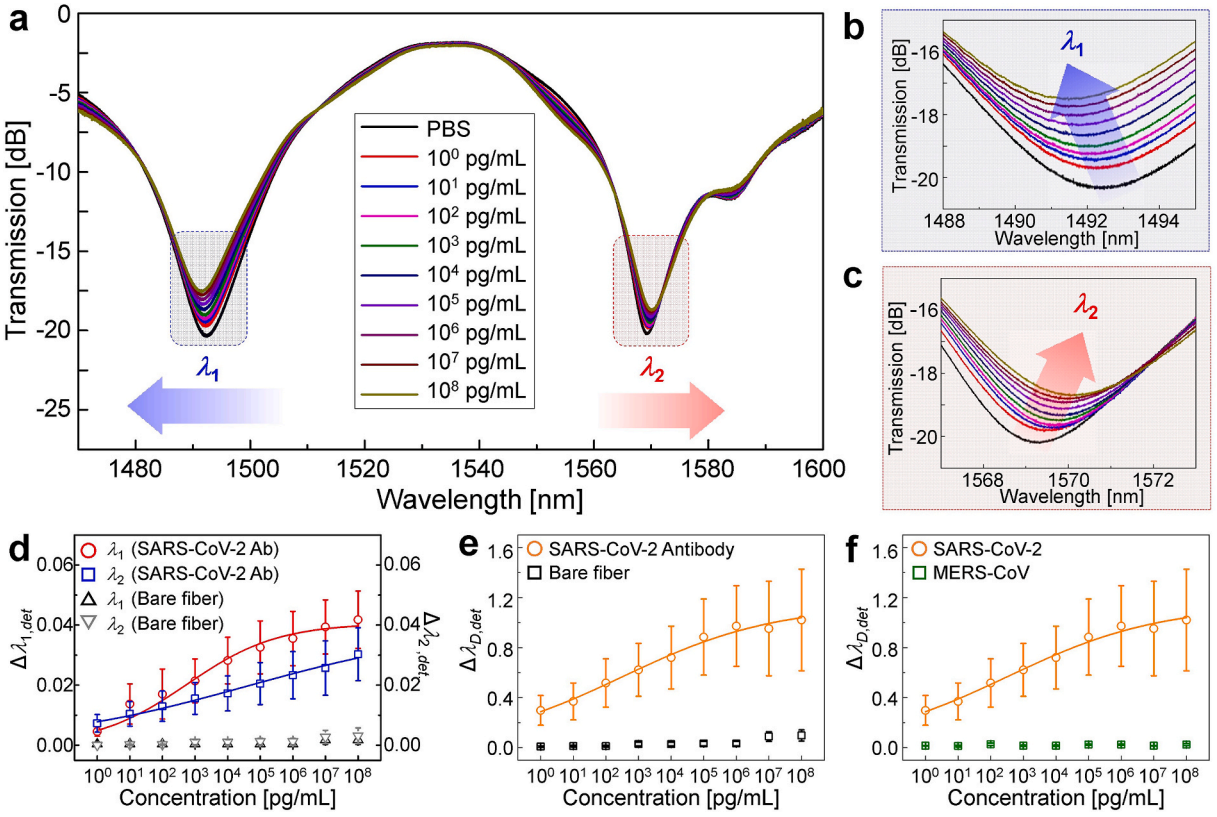

Fig. 4. Sensitive and selective detection of SARS-CoV-2 spike protein. (a) Superposed transmission spectra of SSA-conjugated PS-LPFG, measured for various concentrations (1–10^8 pg/mL) of SARS-CoV-2 spike protein. Magnified plots of (a) near two attenuation dips with dip wavelengths of (b) λ_1 and (c) λ_2, shifting towards shorter and longer wavelength regions with increasing concentration of SARS-CoV-2 spike protein, respectively. (d) Variations of detuning parameters $\Delta\lambda_{1,det}$ and $\Delta\lambda_{2,det}$ of SSA-conjugated PS-LPFG, indicated by red circles and blue squares, respectively, and variations of $\Delta\lambda_{1,det}$ and $\Delta\lambda_{2,det}$ of bare (untreated) PS-LPFG, indicated by black triangles and gray inverted triangles, respectively, according to antigen protein concentration. (e) Variations of $\Delta\lambda_{D,det}$ of SSA-conjugated and bare PS-LPFGs with respect to antigen protein concentration, indicated by orange circles and black squares, respectively. (f) $\Delta\lambda_{D,det}$ variations of SSA-conjugated PS-LPFG according to concentrations of SARS-CoV-2 and MERS-CoV spike proteins, indicated by orange circles and green squares, respectively. All data points related with the SSA-conjugated PS-LPFG, shown in (d), (e), and (f), were nonlinearly fitted based on the Hill adsorption model with a correlation coefficient (R^2) of ~0.99021, and the resulting fitted curves were displayed as solid lines. (For interpretation of the references to colour in this figure legend, the reader is referred to the Web version of this article.)

parameters ($\Delta\lambda_{1,det}$, $\Delta\lambda_{2,det}$, and $\Delta\lambda_{D,det}$) of the untreated (bare) PS-LPFG without SSA conjugation, indicated by black triangles in Fig. 4(d), gray inverted triangles in Fig. 4(d), and black squares in Fig. 4(e), respectively, did not exhibit any remarkable changes for various sample concentrations. The control experiment indicates that SSA is indispensable for specific binding with SARS-CoV-2 spike protein. Thus, in light of the trend of these two responses, our approach exhibits sufficient signal-on/off detection performance, which indicates the "signal-on" at the treated PS-LPFG and the "signal-off" at the untreated one. Regarding the "signal-on" operation, although overlaps between the error bars are responsible for the low measurement resolution, it is possible to differentiate between SARS-CoV-2 spike protein concentrations that differ by more than 10^3 times for sample concentrations less than 10^6 pg/mL. Moreover, to investigate the cross-reactivity of SSA immobilized on the PS-LPFG, we compared its sensitivity to SARS-CoV-2 and MERS-CoV spike proteins. Fig. 4(f) shows the $\Delta\lambda_{D,det}$ variations of the sensor when the concentrations of SARS-CoV-2 and MERS-CoV spike proteins increase from 1 to 10^8 pg/mL, indicated by orange circles and green squares, respectively. As can be confirmed from the figure, no noticeable variations were observed in terms of MERS-CoV spike antigen proteins, suggesting that our SSA-conjugated sensor head is highly specific to SARS-CoV-2 spike proteins.

3.2. Detection of SARS-CoV-2 spike protein in virus transport media

In general, diagnosis of COVID-19 in the clinic is performed using an FA transport medium (FTM), which is used to collect and transport clinical specimens of viruses while sustaining their viability during transit. The FTM includes various reagents such as Hank's balanced salts supplemented with bovine serum albumin, which can affect the sensor performance leading to sensitivity deterioration. To evaluate the detection feasibility of SARS-CoV-2 spike protein in clinical virus transport medium, therefore, we investigated the response of the PS-LPFG sensor to antigens in the FTM. Fig. 5(a) shows the wavelength detuning of λ_D ($\Delta\lambda_{D,det}$) of the sensor, measured using samples (SARS-CoV-2 spike protein) in the PBS and FTM, displayed as blue squares and red circles, respectively. Naturally, the $\Delta\lambda_{D,det}$ magnitude of the sample in the FTM is lower than that of the sample in the PBS because various reagents in the FTM can hinder the interaction between SARS-CoV-2 spike protein and immobilized antibody. Even under the unfavorable conditions, however, the $\Delta\lambda_{D,det}$ signal (indicated by red circles) of the sensor perturbed by SARS-CoV-2 spike protein in the FTM is clearly distinguished from the negative control signal (indicated by black squares) of the sample in the FTM, measured with the bare PS-LPFG without SSA conjugation. The experimental results revealed that the sensor could detect SARS-CoV-2 spike protein at a concentration of 100 pg/mL (as confirmed in Fig. 5(a) and Supplementary Fig. S2). This corroborates that our PS-LPFG sensor can detect antigens in clinical

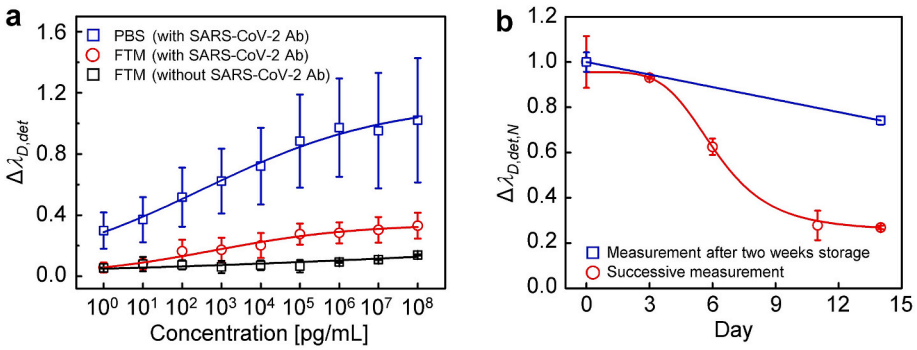

Fig. 5. Practical evaluation of sensing performance. (a) Wavelength detuning of λ_D ($\Delta\lambda_{D,det}$) of the sensor, measured using samples (SARS-CoV-2 spike proteins) in PBS (blue squares) and FTM (red circles). For comparison, the $\Delta\lambda_{D,det}$ signal of the bare PS-LPFG (without SSA conjugation), measured in FTM, is provided as a negative control signal (black squares). (b) Temporal changes in normalized magnitude of $\Delta\lambda_{D,det}$ signal, showing reusability and storage stability of SSA-conjugated PS-LPFG, indicated by red circles and blue squares, respectively. The reusability test was performed using the same sensor head by measuring the $\Delta\lambda_{D,det}$ signal five times for two weeks. The storage stability test was done through measurement of the sensor signal after two weeks of storage. (For interpretation of the references to colour in this figure legend, the reader is referred to the Web version of this article.)

samples without any preprocessing.

3.3. Reusability and storage stability of SSA-conjugated PS-LPFG

In particular, to assess the reusability of the sensor head, repetitive measurements of SARS-CoV-2 spike protein was done using the same sensor head (i.e., SSA-conjugated PS-LPFG) at irregular temporal intervals. As indicated by red circles in Fig. 5(b), the tests were performed by five times for two weeks (14 days). For every test, the sensor head was exposed to SARS-CoV-2 spike protein with a concentration of 1 μg/mL, and the normalized value of $\Delta\lambda_{D,det}$, referred to as $\Delta\lambda_{D,det,N}$, was observed as a sensor signal. Instantly after completing the measurement of the sensor signals, the sensor head was washed with 1 × PBS to remove residue on the sensor surface, which is irrelevant to antibodies and can cause non-specific reactions, and stored at 4 °C in the refrigerator. At the second test (3 days after the first test), the magnitude of the $\Delta\lambda_{D,det,N}$ signal was maintained at 90 % or more. At the third test (6 days after the first test), the magnitude of the signal was maintained at 60 %. So, the measurement reliability might be dropped from the third test. Finally, it was decreased to 30 % or less at the fifth test (14 days after the first test). The decrease in the signal magnitude seems to be caused by the destruction or detachment of SSAs weakly bound to the surface of the sensor head during the washing step. Moreover, the storage stability of the sensor head was also appraised by measuring the sensor signal when exposed to SARS-CoV-2 spike protein two weeks after the initial measurement. Similarly to the case of the reusability assessment, the sensor head was washed with 1 × PBS and stored at 4 °C in the refrigerator, instantly after the initial signal measurement of SARS-CoV-2 spike protein. Then, the next signal measurement was done after two weeks. The measured sensor signals are displayed as blue squares in Fig. 5(b). As can be seen from the figure, our sensor could offer the signal magnitude kept at 70 % or more. This indicates that our sensor can be reused at least one more time within 14 days after the first test, exhibiting reasonable storage stability for a certain period and reliable sensing performance.

3.4. Temperature dependence of SSA-conjugated PS-LPFG

Furthermore, to check whether the sensor performance is affected by ambient temperature changes, we investigated the temperature dependence of the SSA-conjugated PS-LPFG regarding two aspects: (1) Whether antigen-antibody interaction during the sensing operation creates temperature changes on the surface of the sensor head and (2) how the sensor signal is affected by external temperature disturbances. Since the ambient temperature changes can lead to the refractive index changes of the core and cladding of the sensor head as well as the thermal expansion of the buffer solution, it is important to control the ambient temperature and minimize thermally induced noises to accurately measure very small changes in the refractive index occurring in bioassays [22]. While antigen-antibody interaction occurred on the surface of the SSA-immobilized PS-LPFG immersed in the standard buffer solution with a concentration of 1 μg/mL at room temperature, the ambient temperature of the sensor head was monitored using a K-type thermocouple and a digital thermometer with a resolution of 0.1 °C. As seen in Fig. 6(a), the temperature variation near the sensor head within the buffer solution was measured as 0.1 °C during the entire sensing process to detect SARS-CoV-2 spike protein, carried out at room temperature. The actual temperature variation may be less than 0.1 °C because the temperature resolution of the thermometer is 0.1 °C. Next, for scrutinization of the external temperature response of the SSA-conjugated PS-LPFG, it was placed in a temperature chamber, and λ_D of the dual-resonance dips in its transmission spectrum was monitored for the ambient temperature increase (red circles) and decrease (blue squares) in a range of 22–26 °C with a step of 0.5 °C. As seen in Fig. 6(b), the detuning parameter of λ_D, i.e., $\Delta\lambda_{D,det}$, shows no specific temperature dependence. As described earlier, $\Delta\lambda_{D,det}$ was defined as 100 × ($\Delta\lambda_D/\lambda_{D,0}$), where $\lambda_{D,0}$ was set as 91.84 nm because it was the value of λ_D at the onset of the measurement. In the above temperature range, $\Delta\lambda_{D,det}$ was measured as ~0.141 for a temperature change of 4 °C, and, in particular, $\Delta\lambda_{D,det}$ below 0.0218 was observed in a temperature range of 23–24 °C. It can be inferred from this result that, in the room-temperature antigen detection, $\Delta\lambda_{D,det}$ due to temperature perturbations induced by bioaffinity binding is much less than 0.0109. Thus, it is concluded that a λ_D deviation induced by ambient temperature changes rarely affects the measurement accuracy of our antigen detection experiments carried out at room temperature, because the $\Delta\lambda_{D,det}$ value of ~0.0109, obtained by a λ_D deviation of 0.01 nm, is close to the $\Delta\lambda_{D,det}$ magnitude obtained in the bare PS-LPFG. For further implementation of a completely temperature-insensitive system, it is necessary to include a temperature control system based on thermo-electric cooling devices such as Peltier elements in our sensor system [23].

4. Conclusions

In sum, we demonstrated a fiber-optic biosensing platform suited for the label-free detection of SARS-CoV-2 spike protein by employing an SSA-conjugated PS-LPFG as a sensing head to directly detect the bio reaction between bound SSAs and free SARS-CoV-2 spike protein, which induces local changes in the refractive index of a bio-interaction layer deposited on its surface through immobilization of SSAs. A PS-LPFG was fabricated by inserting a π phase shift in the middle of an LPFG inscribed with a CO_2 laser, which results in a splitting of its resonance dip. To achieve high selectivity to SARS-CoV-2 spike protein, its spike antibodies were immobilized on the unjacketed fiber surface of the fabricated PS-LPFG functionalized through chemical modification using

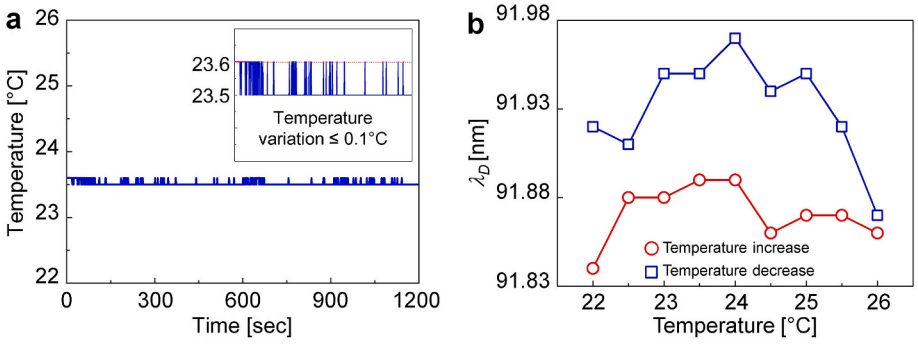

Fig. 6. Temperature dependence of SSA-conjugated PS-LPFG. (a) Temperature variation near sensor head within buffer solution, measured during entire sensing process to detect SARS-CoV-2 spike protein at room temperature. The inset of (a) shows a magnified plot of the measurement result of (a) in a temperature range from 23.3 to 23.7 °C, indicating the temperature variation less than 0.1 °C. (b) Temperature-induced deviations in λ_D of dual-resonance dips of SSA-conjugated PS-LPFG, measured for ambient temperature increase and decrease in a temperature range of 22–26 °C with a step of 0.5 °C, indicated by red circles and blue squares, respectively. (For interpretation of the references to colour in this figure legend, the reader is referred to the Web version of this article.)

APTES and GA. When the SSA-immobilized PS-LPFG was exposed to SARS-CoV-2 spike protein, λ_D varied with increasing antigen concentration owing to bioaffinity binding-induced changes in the refractive index at its surface. Through quantitative analysis of λ_D as a function of the binding event between antigen and antibody at the fiber surface, we could detect SARS-CoV-2 spike protein with the proposed sensor not only in the standard buffer but also in virus transport medium. Moreover, our sensor could discriminate SARS-CoV-2 spike protein from those of MERS-CoV and also offer the reusability and storage stability of the sensor head. Furthermore, we confirmed that the temperature-induced measurement uncertainty was negligible in the room-temperature antigen detection. As a result, the SSA-conjugated PS-LPFG can act as an optical transducer capable of sensitive and selective detection of SARS-CoV-2 spike protein in a clinical virus transport medium as well as a standard buffer. Findings from this study highlight the potential of the SSA-immobilized PS-LPFG for the development of the immunological diagnosis of COVID-19, and we wish our cost-effective fiber-optic biosensor to be a step forward for the rapid extinction of the global pandemic.

Funding

This research was supported by Basic Science Research Program through the National Research Foundation (NRF-2019R1I1A3A01046232) funded by the Ministry of Education and the National Research Foundation (NRF-2020M3E9A1043749) funded by the Ministry of Science and ICT, Republic of Korea.

Declaration of competing interest

The authors declare that they have no known competing financial interests or personal relationships that could have appeared to influence the work reported in this paper.

Acknowledgments

This work was presented as a part of the Ph.D. dissertation of S.-L. Lee, Pukyong National University, Busan, South Korea, 2021.

Appendix A. Supplementary data

Supplementary data to this article can be found online at https://doi.org/10.1016/j.talanta.2021.122801.

Credit author statement

Seul-Lee Lee: Conceptualization, Methodology, Investigation, Data curation, Writing – original draft. **Jihoon Kim:** Software, Methodology. **Sungwook Choi:** Data curation, Methodology. **Jinsil Han:** Investigation, Data curation. **Giwan Seo:** Conceptualization, Methodology, Validation, Data curation, Writing – original draft. **Yong Wook Lee:** Supervision, Project administration, Funding acquisition, Conceptualization, Methodology, Writing – review & editing.

References

[1] A.S. Fauci, H.C. Lane, R.R. Redfield, Covid-19 — navigating the uncharted, N. Engl. J. Med. 382 (2020) 1268–1269, https://doi.org/10.1056/NEJMe2002387.
[2] WHO, Weekly Operational Update on COVID-19, 2020 (accessed March 4, 2021).
[3] Z. Zhao, H. Cui, W. Song, X. Ru, W. Zhou, X. Yu, A Simple Magnetic Nanoparticles-Based Viral RNA Extraction Method for Efficient Detection of SARS-CoV-2, bioRxiv, 2020, https://doi.org/10.1101/2020.02.22.961268.
[4] L. Yu, S. Wu, X. Hao, X. Dong, L. Mao, V. Pelechano, W.-H. Chen, X. Yin, Rapid detection of COVID-19 coronavirus using a reverse transcriptional loop-mediated isothermal amplification (RT-LAMP) diagnostic platform, Clin. Chem. 66 (2020) 975–977, https://doi.org/10.1093/clinchem/hvaa102.
[5] G. Qiu, Z. Gai, Y. Tao, J. Schmitt, G.A. Kullak-Ublick, J. Wang, Dual-functional plasmonic photothermal biosensors for highly accurate severe acute respiratory syndrome coronavirus 2 detection, ACS Nano 14 (2020) 5268–5277, https://doi.org/10.1021/acsnano.0c02439.
[6] P.D. Tam, M.A. Tuan, T.Q. Huy, A.T. Le, N.V. Hieu, Facile preparation of a DNA sensor for rapid herpes virus detection, Mater. Sci. Eng. C 30 (2010) 1145–1150, https://doi.org/10.1016/j.msec.2010.06.010.
[7] G. Seo, G. Lee, M.J. Kim, S.-H. Baek, M. Choi, K.B. Ku, C.-S. Lee, S. Jun, D. Park, H. G. Kim, S.-J. Kim, J.-O. Lee, B.T. Kim, E.C. Park, S.I. Kim, Rapid detection of COVID-19 causative virus (SARS-CoV-2) in human nasopharyngeal swab specimens using field-effect transistor-based biosensor, ACS Nano 14 (2020) 5135–5142, https://doi.org/10.1021/acsnano.0c02823.
[8] F. Baldini, M. Brenci, F. Chiavaioli, A. Giannetti, C. Trono, Optical fibre gratings as tools for chemical and biochemical sensing, Anal. Bioanal. Chem. 402 (2012) 109–116, https://doi.org/10.1007/s00216-011-5492-3.
[9] P. Pilla, P.F. Manzillo, V. Malachovska, A. Buosciolo, S. Campopiano, A. Cutolo, L. Ambrosio, M. Giordano, A. Cusano, Long period grating working in transition mode as promising technological platform for label-free biosensing, Opt Express 17 (2009), https://doi.org/10.1364/OE.17.020039, 20039–20050.
[10] V. Mishra, N. Singh, U. Tiwari, P. Kapur, Fiber grating sensors in medicine: current and emerging applications, Sens. Actuators A Phys. 167 (2011) 279–290, https://doi.org/10.1016/j.sna.2011.02.045.
[11] Z. Wang, J.R. Heflin, K. Van Cott, R.H. Stolen, S. Ramachandran, S. Ghalmi, Biosensors employing ionic self-assembled multilayers adsorbed on long-period fiber gratings, Sensor. Actuator. B Chem. 139 (2009) 618–623, https://doi.org/10.1016/j.snb.2009.02.073.
[12] T. Erdogan, Fiber grating spectra, J. Lightwave Technol. 15 (1997) 1277–1294, https://doi.org/10.1109/50.618322.
[13] H.J. Patrick, A.D. Kersey, F. Bucholtz, Analysis of the response of long period fiber gratings to external index of refraction, J. Lightwave Technol. 16 (1998) 1606–1612, https://doi.org/10.1109/50.712243.
[14] C. Liu, Q. Cai, B. Xu, W. Zhu, L. Zhang, J. Zhao, X. Chen, Graphene oxide functionalized long period grating for ultrasensitive label-free immunosensing, Biosens. Bioelectron. 94 (2017) 200–206, https://doi.org/10.1016/j.bios.2017.03.004.
[15] A. Deep, U. Tiwari, P. Kumar, V. Mishra, S.C. Jain, N. Singh, P. Kapur, L. M. Bharadwaj, Immobilization of enzyme on long period grating fibers for sensitive glucose detection, Biosens. Bioelectron. 33 (2012) 190–195, https://doi.org/10.1016/j.bios.2011.12.051.
[16] S.M. Tripathi, W.J. Bock, P. Mikulic, R. Chinnappan, A. Ng, M. Tolba, M. Zourob, Long period grating based biosensor for the detection of Escherichia coli bacteria, Biosens. Bioelectron. 35 (2012) 308–312, https://doi.org/10.1016/j.bios.2012.03.006.
[17] M. Janczuk-Richter, M. Dominik, E. Roźniecka, M. Koba, P. Mikulic, W.J. Bock, M. Łoś, M. Śmietana, J. Niedziółka-Jönsson, Long-period fiber grating sensor for detection of viruses, Sensor. Actuator. B Chem. 250 (2017) 32–38, https://doi.org/10.1016/j.snb.2017.04.148.

[18] X.L. Li, W.G. Zhang, J. Ruan, S.S. Zhang, Temperature-and strain-insensitive torsion sensor based on phase-shifted ultra-long-period grating, Electron. Lett. 48 (2012) 235–236, https://doi.org/10.1049/el.2013.1229.
[19] P. Wang, L. Xian, H. Li, Fabrication of phase-shifted long-period fiber grating and its application to strain measurement, IEEE Photon. Technol. Lett. 27 (2014) 557–560, https://doi.org/10.1109/lpt.2014.2385067.
[20] Y. Zhu, P. Shum, X. Chen, C.H. Tan, C. Lu, Resonance-temperature-insensitive phase-shifted long-period fiber gratings induced by surface deformation with anomalous strain characteristics, Opt. Lett. 30 (2005) 1788–1790, https://doi.org/10.1364/OL.30.001788.
[21] R. Garg, S.M. Tripathi, K. Thyagarajan, W.J. Bock, Long period fiber grating based temperature-compensated high performance sensor for bio-chemical sensing applications, Sensor. Actuator. B Chem. 176 (2013) 1121–1127, https://doi.org/10.1016/j.snb.2012.08.059.
[22] C. Trono, F. Baldini, M. Brenci, F. Chiavaioli, M. Mugnaini, Flow cell for strain-and temperature-compensated refractive index measurements by means of cascaded optical fibre long period and Bragg gratings, Meas. Sci. Technol. 22 (2011), 075204, https://doi.org/10.1088/0957-0233/22/7/075204.
[23] F. Esposito, L. Sansone, A. Srivastava, F. Baldini, S. Campopiano, F. Chiavaioli, M. Giordano, A. Giannetti, A. Iadicicco, Long period grating in double cladding fiber coated with graphene oxide as high-performance optical platform for biosensing, Biosens. Bioelectron. 172 (2021) 112747, https://doi.org/10.1016/j.bios.2020.112747.